RELATIONSHIPS BETWEEN FLUID VORTICITY, KINETIC HELICITY, AND MAGNETIC FIELD ON SMALL-SCALES (QUIET-NETWORK) ON THE SUN

C. R. SANGEETHA AND S. P. RAJAGURU
Indian Institute of Astrophysics, Bangalore-34, India; crsangeetha@iiap.res.in

ABSTRACT

We derive horizontal fluid motions on the solar surface over large areas covering the quiet-Sun magnetic network from local correlation tracking of convective granules imaged in continuum intensity and Doppler velocity by the Helioseismic and Magnetic Imager (HMI) on board the *Solar Dynamics Observatory*. From these we calculate the horizontal divergence, the vertical component of vorticity, and the kinetic helicity of fluid motions. We study the correlations between fluid divergence and vorticity, and between vorticity (kinetic helicity) and the magnetic field. We find that the vorticity (kinetic helicity) around small-scale fields exhibits a hemispherical pattern (in sign) similar to that followed by the magnetic helicity of large-scale active regions (containing sunspots). We identify this pattern to be a result of the Coriolis force acting on supergranular-scale flows (both the outflows and inflows), consistent with earlier studies using local helioseismology. Furthermore, we show that the magnetic fields cause transfer of vorticity from supergranular inflow regions to outflow regions, and that they tend to suppress the vortical motions around them when magnetic flux densities exceed about 300 G (from HMI). We also show that such an action of the magnetic fields leads to marked changes in the correlations between fluid divergence and vorticity. These results are speculated to be of importance to local dynamo action (if present) and to the dynamical evolution of magnetic helicity at the small-scale.

Key words: Sun: granulation – Sun: magnetic fields – Sun: photosphere

1. INTRODUCTION

Interactions between turbulent convection and magnetic fields in the photospheric layers of the Sun play central roles in structuring and driving varied forms of dynamical phenomena in the atmospheric layers above, and hence in the energetics (see, e.g., Nordlund et al. 2009 and references therein). These interactions in the near-surface layers are also basic to local dynamo action (Schussler & Vogler 2008), which, if present, could explain the large amount of quiet-Sun magnetic flux inferred from high-resolution observations (Lites et al. 2008; Goode et al. 2010). An important aspect of these interactions is the role of helical or swirly fluid motions which can similarly twist or inject helicity to the magnetic field, and vice versa. Helicity of a vector field, in general, is defined as the volume integral of the scalar product of the field vector and its curl (or rotation) and it quantifies the amount of twistedness in the vector field (Berger & Field 1984). For fluid flow, the kinetic helicity, H_k, is such a quantity derived from velocity v and its curl or vorticity, $\boldsymbol{\omega} = \nabla \times \boldsymbol{v}$: $H_k = \int \boldsymbol{v} \cdot \boldsymbol{\omega} dV$, where dV is the volume element. For magnetic fields, helicity can be calculated in two different ways (Pevtsov et al. 1995): the magnetic helicity, in general, is obtained by applying the above definition on the vector potential $\boldsymbol{A}$ and its curl (i.e., the magnetic field $\boldsymbol{B} = \nabla \times \boldsymbol{A}$), $H_m = \int \boldsymbol{A} \cdot \nabla \times \boldsymbol{A} dV$; and use of the magnetic field and its curl in the above definition gives the so-called current helicity, $H_c = \int \boldsymbol{B} \cdot \nabla \times \boldsymbol{B} dV$. Both H_m and H_c are measures of twistedness in the magnetic field, and they normally preserve signs over a volume of physical interest (Seehafer 1990; Pevtsov et al. 1995). Interactions between kinetic and magnetic helicities play fundamental roles in magnetic field generation (or dynamo action) as well as in the magneto-hydrodynamical evolution of the fluid and magnetic fields (Parker 1955; Moffat 1978; Krause & Rädler 1980; Brandenburg & Subramanian 2005).

The helicities (magnetic and kinetic) of solar active regions have been extensively studied using observations of the magnetic and velocity fields in and around them. A well known property of the active region magnetic fields is the hemispheric sign rule, originally discovered by Hale (1927) (see also, Seehafer 1990; Pevtsov et al. 1995); active regions in the northern hemisphere show a preferential negative magnetic helicity while those in the southern hemisphere show positive helicity. The origin or exact cause of such a pattern in large-scale magnetic helicity is still not fully understood. Dynamo mechanisms that impart helicity while the field is being generated, as well as the transfer of kinetic helicity from fluid motions to the magnetic field as it rises through the convection zone (Longcope et al. 1998) or during and after its emergence at the surface (photosphere), are thought to play roles in the observed pattern (Liu et al. 2014a). On the small-scale,[1] away from the active and emerging flux regions, the magnetic and kinetic helicities and their interactions are even more poorly understood, as measuring them reliably poses significant difficulties. Although significant advances have been made in mapping horizontal velocities through correlation tracking of surface features such as granulation or magnetic structures (e.g., see Welsch et al. 2007 and references therein), significant uncertainties remain in measuring horizontal components of vector magnetic field at the small-scale (Hoeksema et al. 2014; Liu et al. 2014b) and hence in estimating reliably the current or magnetic helicities there (Y. Liu 2015, private communication; A. Norton, 2016 private communication; see further discussion below.). Observational studies by Duvall & Gizon (2000) and

---

[1] "Large-scale" and "small-scale" are defined, for the purposes of this paper, to represent the spatial sizes of coherent magnetic structures: large magnetic structures such as sunspots are "large-scale," while the smaller structures outlining supergranular boundaries are "small-scale." It should be noted, however, that these small magnetic structures are distributed on a large-scale all over the solar surface.

Gizon & Duvall (2003) have explored vertical vorticities associated with supergranular-scale flows and such results have guided some theoretical studies of the relations between kinetic and magnetic helicities in the context of turbulent dynamo mechanisms (Rudiger 2001; Rudiger et al. 2001).

Apart from the above described aspects of interactions between fluid motions and the magnetic field, recently, vortex motions around small-scale magnetic flux tubes and the transfer of helicity from fluid motions to magnetic fields have been identified as key players in the upward energy transport and thus in the heating of solar corona (Wedemeyer-Bohm et al. 2012). While Wedemeyer-Bohm et al. (2012) found vortex flows with lifetimes of about an hour, the numerical simulations of Shelyag et al. (2013) show no long-lived vortex flows in the solar photosphere. Detection of vortex flows at the granular scale in the photosphere date back to the studies by Brandt et al. (1988) and Simon et al. (1989), who inferred that such motions could be common features in the granular and supergranular inflow regions. A slightly excess correlation between negative divergence of the horizontal flows (or inflows) and vertical vorticity was found by Wang et al. (1995). Bonet et al. (2008) detected a large number of small vortices in the inflow regions and found a clear association between them and magnetic bright points. Innes et al. (2009) have detected vorticites in the inflow regions by calculating horizontal flows using a ball-tracking technique. Balmaceda et al. (2010) detected strong magnetic flux at the centers of the vortex flows. Vortical flow maps in the quiet-Sun were calculated by Komm et al. (2007) and the circular flow components of the inflows around active regions were calculated by Hindman et al. (2009) using a helioseismic ring-diagram technique. A recent work has compared spatially resolved vertical vorticites calculated from two independent techniques, local correlation tracking (LCT) and time-distance helioseismology (Langfellner et al. 2015).

Despite a good number of studies on the vortex flows themselves, there have not been detailed analyses of the relationships between such fluid motions and the magnetic field at the small-scale. For example, there are no reliable inferences on the connections between the helicities of fluid motion and the magnetic field, and on the back-reaction of the magnetic field on the fluid. Much of the difficulty lies in reliably measuring the H_m or H_c of the small-scale magnetic fields, as vector field measurements are often subject to large uncertainties outside sunspots or active regions (Hoeksema et al. 2014; Liu et al. 2014b). For these reasons, there are no reliable measurements to ascertain if the helicity of small-scale magnetic fields follows the hemispheric sign pattern obeyed by active regions. There are conflicting findings regarding the dominant signs of current helicity in the weak or small-scale fields over the hemispheres (Zhang 2006; Gosain et al. 2013). Helioseismology results on supergranular-scale flows, however, show the effect of Coriolis force introducing a hemispheric sign pattern in the vorticity (and hence kinetic helicity) of such flows (Duvall & Gizon 2000; Gizon & Duvall 2003; Gizon & Birch 2005; Komm et al. 2014; Langfellner et al. 2015).

In this work, we focus on examining how the magnetic field modifies the relationships among the fluid dynamical quantities, divergence, vorticity, and kinetic helicity on the one hand, and how these quantities themselves scale against the strength of the magnetic field on the other. Such an analysis is facilitated by the continuous full-disk coverage of the Sun in velocity (Doppler), granulation (continuum intensity), and magnetic field provided by the Helioseismic and Magnetic Imager (HMI) on board the *Solar Dynamics Observatory* (*SDO*; Schou et al. 2012). Although the spatial resolution of about 1 arcsec (about 720 km) provided by HMI enables us to track the granulation features in both the continuum and velocity images, and to derive the horizontal flow field, it is not sufficient to resolve the sub-granular scale vortex flows that possibly surround the tiny magnetic flux concentrations. Hence, the vertical vorticity that we measure from HMI data through LCT of granular motions would have contributions mainly from vortical flows the size of several granules. Since such flows are likely dominant at the supergranular boundaries and junctions we, in our analyses here, are able to also study the effects of the Coriolis force (Duvall & Gizon 2000; Gizon & Duvall 2003) and their influence on the relations between vortex motions and magnetic fields. We discuss the data and the analysis methods in Section 2, the results in Section 3, and provide discussion, conclusions, and notes on future studies in Section 4.

2. DATA AND ANALYSIS METHODS

We have used the three major observables from the HMI on board the *SDO*: Doppler velocities (v_d), continuum intensities (I_c), and line-of-sight (LOS) magnetic fields B_{LOS} (hereafter, we denote B_{LOS} simply as B). The basic data sets are cubes of the above observables over about 19 large regions, typically $30°7 \times 30°7$ in size (in heliographic degrees, or $373 \times 373\,\mathrm{Mm}^2$ with $0°03\,\mathrm{pixel}^{-1}$) covering both the northern and southern hemispheres in the latitude range $\pm30°$ and about $\pm15°$ in longitude about the central meridian, tracked for 14 hr and remapped (Postel projected) to a uniform pixel size of $0''5\,\mathrm{pixel}^{-1}$. The total area covered by the 19 regions on the solar surface is $19 \times 373 \times 373\,\mathrm{Mm}^2 = 2.65 \times 10^6\,\mathrm{Mm}^2$, which is about 0.87 solar hemispheres. The 19 regions chosen are from 11 dates distributed over the years 2010–2012. On each of the eight dates, 2010 July 11, August 3, October 8, and November 3, and 2011 February 8, February 19, July 3, and October 2, we have two regions, one centered at 15°N and the other centered at 15°S, and with central longitudes within about 15° of the central meridian. On the dates 2012 May 8, 2011 June 21 and July 2, three regions centered at 0° latitude and the central meridian were included. Thus the included regions cover equal amount of northern and southern hemispherical areas. Of the 19 regions, 14 are quiet-network regions chosen by examining the magnetograms for the presence of a mixed-polarity network field well away from active regions. The remaining five regions on the five dates, 2010 August 3, 2011 February 19, July 3, October 2, and 2012 July 2, however, have a sunspot; the data from the first four regions were already available to us and had been used in a different analysis published by the second author (Rajaguru et al. 2013). We included quiet areas of these regions by carefully excluding the sunspots and surrounding plages (one example is shown Figure 1) covering about 8% of the total area, and hence the total quiet-network area included in the analysis is about 0.8 solar hemispheres. Since this discarded area of about 0.07 solar hemispheres is all from the north, we have about 15% more southern hemispherical area than northern in the analyses here. Figure 1 shows two examples from among the analyzed regions: derived flow divergence and vorticity maps overlaid with magnetic field contours (see the following section) over a
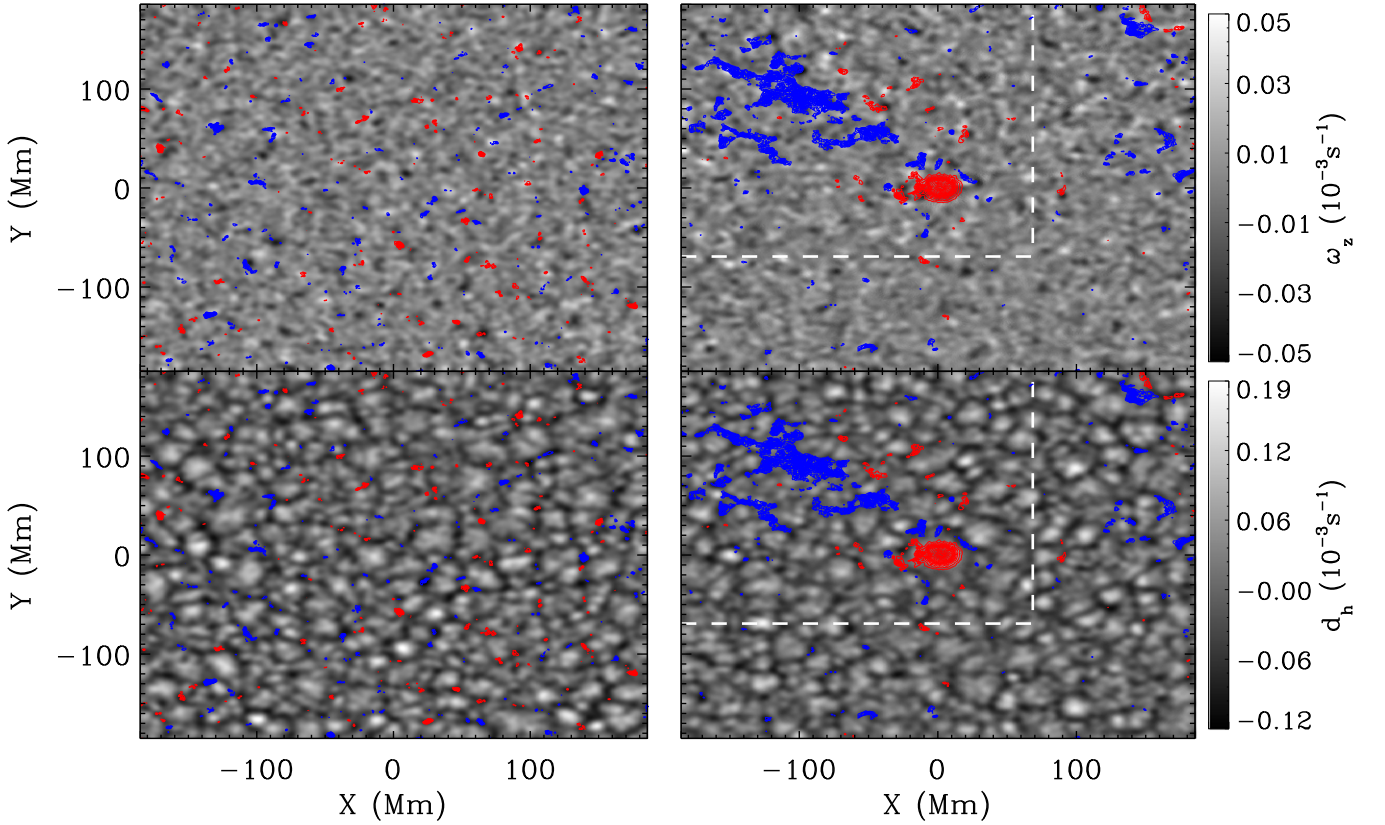
Figure 1. Spatial maps of 14 hr averaged vertical vorticities (top panels) and horizontal divergences (bottom panels) derived from LCT of HMI Doppler velocities. The left panels show a region consisting of mixed-polarity quiet-network magnetic fields observed on 2010 November 3 with the map center at latitude 15°S and longitude 0°; the right panels show a sunspot region observed on 2010 August 3 centered at latitude 15°N and longitude 0°. Contours of the magnetic fields averaged in the same way are overplotted, showing field values above ±10 G. The red and blue contours correspond to negative and positive magnetic polarity magnetic fields, respectively. The white dotted lines in the right-hand panels separate the sunspot and plage areas from the quiet-network, which is used in the work presented here.

mixed-polarity quiet-network area (left panels) and over a region covering a sunspot and plages (right panels). The white-line boundaries in the right panel of Figure 1 separate the quiet-Sun areas included in the analysis for this region, and these were chosen by visually examining the magnetograms to avoid sunspots and surrounding plages and to include only the quiet-Sun network. These straight-line boundaries are just for convenience and easy inclusion of the chosen areas in the analyses.

We apply the LCT technique (November & Simon 1988) on v_d and I_c to derive horizontal motions of convective granules. We use the code FLCT (Welsch et al. 2004) that implements LCT through measurement of correlation shifts in the Fourier space. FLCT is applied for two images separated by a time $\triangle t$. Each image is multiplied by a Gaussian of width σ centered at the pixel where velocity has to be derived. Cross-correlation is performed within this Gaussian window to calculate the shifts in the x- and y-directions that maximize the correlation. The shifts in the x- and y-directions are divided by $\triangle t$ to obtain velocities in the x- and y-directions. We remove the f (surface gravity) and p mode oscillation signals in v_d and I_c before applying the LCT to derive fluid motions. This is achieved using a Gaussian tapered Fourier frequency filter that removes frequency components above 1.2 mHz. The FWHM of the Gaussian window for LCT is $\sigma = 15$ pixels and $\triangle t$ is about 2 minute. We apply FLCT at every time-step, i.e., every 45 s, to derive the horizontal velocity components $v_x(x, y, t)$ and $v_y(x, y, t)$ with the original resolution of the data. From these horizontal

components of velocity, we calculate the z-component of the vorticity and the horizontal divergence as,

$$(\boldsymbol{\nabla} \times \boldsymbol{v})_z = \left(\frac{\partial v_y}{\partial x} - \frac{\partial v_x}{\partial y} \right), \tag{1}$$

$$(\boldsymbol{\nabla} \cdot \boldsymbol{v})_h = \left(\frac{\partial v_x}{\partial x} + \frac{\partial v_y}{\partial y} \right). \tag{2}$$

Calculation of kinetic helicity H_k requires the vertical component of $\boldsymbol{v}$ and its gradient, which we do not have. We follow (Rudiger et al. 1999) in deriving a proxy for kinetic helicity from the calculated vertical component of vorticity and horizontal divergence,

$$H_{k,\text{proxy}} = \frac{\langle (\boldsymbol{\nabla} \cdot \boldsymbol{v})_h (\boldsymbol{\nabla} \times \boldsymbol{v})_z \rangle}{\langle (\boldsymbol{\nabla} \cdot \boldsymbol{v})_h)^2 \rangle^{1/2} \langle (\boldsymbol{\nabla} \times \boldsymbol{v})_z)^2 \rangle^{1/2}}. \tag{3}$$

This proxy for kinetic helicity is similar to the relative kinetic helicity, $H_{k,\text{rel}}$, used by Brandenburg et al. (1995)

$$H_{k,\text{rel}} = \frac{\langle \boldsymbol{\omega} \cdot \boldsymbol{v} \rangle}{\langle \omega^2 \rangle^{1/2} \langle v^2 \rangle^{1/2}}. \tag{4}$$

in situations dominated by two-dimensional flows.

3

3. RESULTS: VORTICAL MOTIONS, KINETIC HELICITY, AND THE MAGNETIC FIELD

Spatial maps of horizontal divergence, $d_h = (\nabla \cdot v)_h$, the vertical vorticity $\omega_z = (\nabla \times v)_z$, and the kinetic helicity H_k (hereafter we denote $H_{k,proxy}$ defined above simply as H_k), derived at each time-step as described in the previous section, form our basic fluid dynamical quantities. To improve the signal-to-noise of these measurements, we use a running temporal average over about 4.5 minutes, i.e., an average of six individual measurements; this is found to be suitable as the typical lifetime of granules is about 5–7 minutes. This running average is taken on the flows derived but not on the cross-correlations of LCT to avoid missing any granular signals that have lifetimes shorter than or close to the averaging interval. An example map of the full 14 hr temporal average of d_h and ω_z with overlaid contours of similarly averaged B is shown in Figure 1.

The velocity maps v_x and v_y calculated from Doppler observations show a systematic variation in the x- and y-directions, and the magnitude of change across the spatial extent covered is about $0.4\,\mathrm{ms^{-1}}$. This is attributed to the "shrinking Sun effect" (Lisle & Toomre 2004; Langfellner et al. 2015) that shows an apparent disk-centered (or radially directed) inflow. The origin of this constant flow signal (i.e., time independent) is not fully known, although it has been attributed to selection bias of the LCT method and to insufficient resolution of the instrument to resolve fully the granules on the solar surface (Lisle & Toomre 2004). Whatever the origin, this constant disk-centered flow signal is easily determined by taking temporal averages (of both v_x and v_y), spatially smoothing and obtaining a low degree 2D fit. A thus determined background artifact is then removed by subtracting it from maps v_x and v_y at every time-step.

In this study, we examine (1) the hemispherical dependence of the signs of ω_z or H_k arising from the Coriolis force, (2) how the magnetic field modifies the relationship between d_h and ω_z or H_k, and (3) how these quantities themselves scale against the strength of the magnetic field. Since these quantities are highly dynamic with typical timescales of the order of granular lifetime, we derive the relationship between these quantities at each time-step of measurement. We achieve this by determining, at each time-step, the dependence of ω_z (or H_k) on d_h and B by calculating their average values over chosen small intervals (bin sizes) in B and d_h: $10\,\mathrm{G}^2$ bins in B (a magnetic bin) and $20\,\mu\mathrm{s}^{-1}$ bins in d_h. This is implemented by sub-dividing every magnetic bin, i.e., pixels having a magnetic field spread of $10\,\mathrm{G}$, in terms of d_h with a bin size of $20\,\mu\mathrm{s}^{-1}$. We do this for both signed and absolute values of ω_z or H_k, denoting them respectively as $\omega_z(d_h, B)$ or $H_k(d_h, B)$, and $\omega_z^{ab}(d_h, B)$ or $H_k^{ab}(d_h, B)$; in the former case of averages of signed values we perform the calculations for the northern and southern hemispheric regions separately so as to check the hemispheric trends such as those introduced by the Coriolis force, and in the latter case of average of absolute values we combine both hemispheric regions together. The fill-factor for the magnetic field is

small (i.e., much of the area is occupied by $|B| \approx 0\,\mathrm{G}$ pixels, see to Figure 1) and, in general, the area occupied by magnetic pixels decreases sharply as $|B|$ increases (see the bottom panel of Figure 3, where a histogram of area, in logarithmic scale, against B is plotted). In such situations a better statistic is provided by median values rather than averages. We tested this by taking median values over the chosen bins of B and d_h and found, however, that the derived relationships are nearly the same for averages and medians.

The above analysis process is repeated for each region, and the average $\omega_z(d_h, B)$, $\omega_z^{ab}(d_h, B)$, $H_k(d_h, B)$, and $H_k^{ab}(d_h, B)$ are thus determined from for all the regions, making sure that the included areas contain only the quiet-Sun magnetic network. The resulting average relationships $\omega_z(d_h, B)$ and $H_k(d_h, B)$ determined for the northern and southern hemispheric regions separately are shown in Figures 2 and 3: results based on LCT velocities derived using HMI continuum intensities I_c are in Figure 2 and those from Doppler velocities are in Figure 3, and they agree well. It is seen that the Doppler velocities yield somewhat less noisy results for $\omega_z(d_h, B)$ and $H_k(d_h, B)$ and hence we use these for further analyses in the following sections. It is to be noted that the signed averages $\omega_z(d_h, B)$ ($H_k(d_h, B)$) have cancellations and hence measure only the excess of one sign of rotation (either clockwise (negative) or counter-clockwise (positive) rotation) over the other. Hence, the vanishing of these averages does not necessarily mean absence of rotations, and this is easily checked by the averages of the absolute values of $\omega_z^{ab}(d_h, B)$ ($H_k^{ab}(d_h, B)$) shown in Figures 6 and 7 (a full discussion of results in these figures is deferred to Section 3.1). As can clearly be seen, the excesses $\omega_z(d_h, B)$ ($H_k(d_h, B)$) of one sign over the other are about one-tenth of $\omega_z^{ab}(d_h, B)$ ($H_k^{ab}(d_h, B)$). Further, we see that such cancellations are the largest for non-magnetic (quiet) flows. The dominance of one sign of $\omega_z(d_h, B)$ for flows around magnetized regions is due to the phenomenon of flux expulsion (Proctor & Weiss 1982) which leads to magnetic flux occupying preferentially the inflow (negative d_h) locations. We discuss this aspect further in the following section.

3.1. Vorticity–Divergence Correlation: the Effects of the Coriolis Force

The results in Figures 2 and 3 show that, to a large extent, the sign of ω_z (H_k) is positive (negative) or counter-clockwise rotation in the northern hemisphere, and negative (positive) or clockwise rotation in the southern hemisphere. It should be noted that, in the absence of Coriolis and any other large-scale force, the flows are expected to have a roughly equal distribution of clockwise (negative) and counter-clockwise rotations, and hence a signed average of ω_z or H_k over the magnetic and divergence bins is expected to yield near-zero values due to cancellation among positive and negative vorticities. However, as earlier studies have shown, super-granular-scale flows are indeed subject to Coriolis force and, as the results in Figures 2 and 3, show that even the smaller-sized inflows (negative d_h) show a predominant hemispheric sign pattern consistent with the Coriolis effect. A closer look at this striking pattern requires understanding first the d_h–ω_z relationship for the non-magnetic flows.

Quiet-Sun areas devoid of significant magnetic field are captured in the central vertical area close to $|B| = 0\,\mathrm{G}$ in Figures 2 and 3. We take the average of ω_z within $|B| < 15\,\mathrm{G}$,

---

[2] We note that the use of $B = B_{LOS}$ leads to, when much of the magnetic field is vertically oriented on the surface, a systematic bias toward lower field strengths that are about $\cos(\theta)$ times the true value for an angular distance of $\theta°$ from the disk center. Since the maximum off-center location does not exceed $\theta = 30°$, we have at the most 14% lower values for B. However, average deviations of derived dependences on $B = B_{LOS}$ would differ from the true values of B by a much smaller amount than 14%.
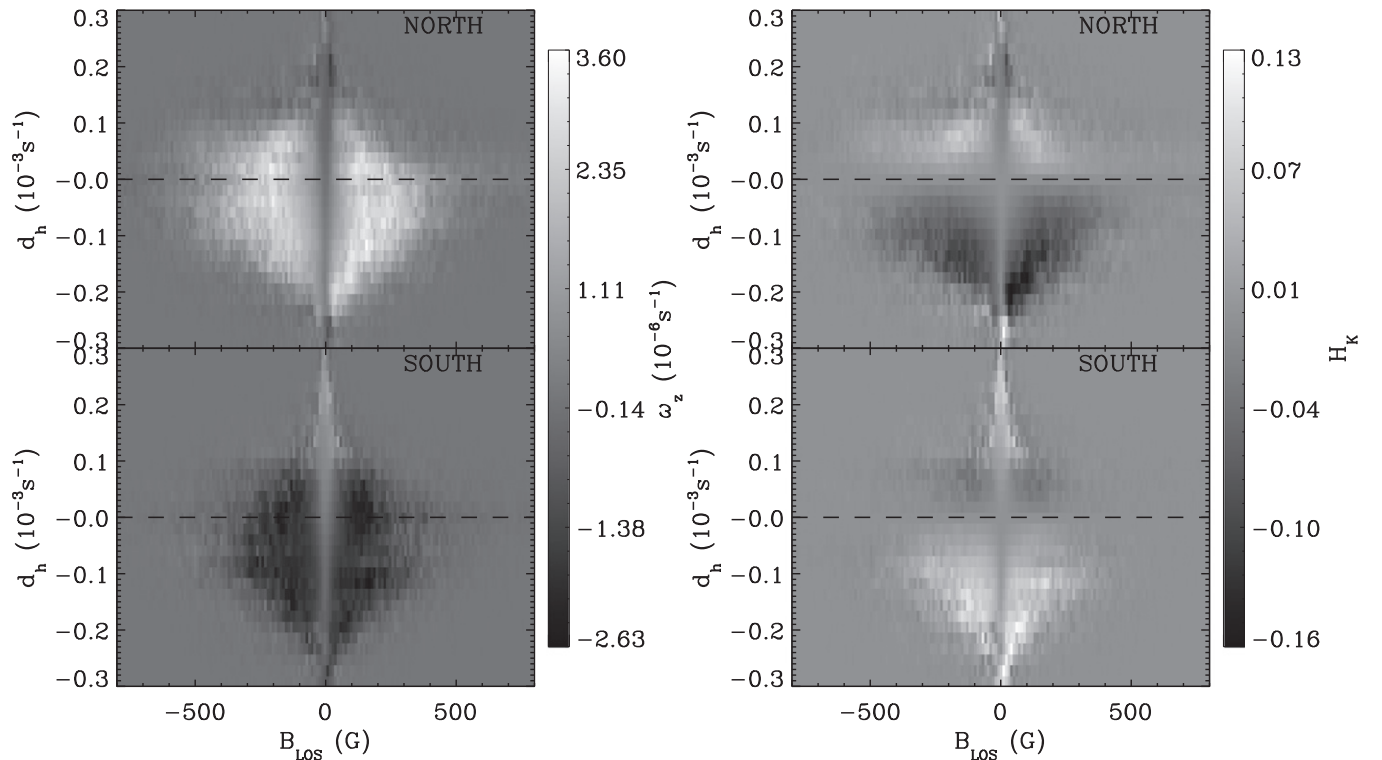
Figure 2. Vertical (z-component) vorticity, $\omega_z(d_h, B)$ (left panels), and kinetic helicity, $H_k(d_h, B)$ (right panels), binned against LOS magnetic field, B (x-axis), and horizontal divergence, d_h (y-axis). The results here are calculated from LCT of granular motions imaged in HMI continuum intensities, and are averages over the quiet-network in 19 large regions covering the northern and southern hemispheres. See the text for further details.

i.e., a horizontal average over three magnetic bins of -10, 0, and 10 G in Figure 3, to determine $\omega_z^q(d_h) = \omega_z(d_h, B = 0)$ for the non-magnetic flows. It should be noted that the observational errors in HMI LOS magnetograms are about 10 G (Scherrer et al. 2012) and hence the pixels within $|B| < 15$ G can be considered as non-magnetic. The resulting variation of $\omega_z^q(d_h)$ is shown as blue lines in Figure 4 (the other colored lines in this figure show averages over different ranges of $|B|$, and we discuss them in the following section). Signed values of ω_z against d_h are shown in the left panel of Figure 4, and a comparison of absolute amplitudes of ω_z at inflows and outflows is shown in the right panel by plotting them against absolute d_h. Results plotted similarly for H_k are shown in Figure 5. In these figures, we show only the results obtained from LCT velocities derived using HMI Doppler velocities (results obtained from HMI I_c are very similar). The variation of $\omega_z^q(d_h)$ clearly brings out the effect of the Coriolis force on fluid flows on the supergranular-scale, namely a radial outflow (positive d_h) rotates clockwise (negative ω_z) and a inflow (negative d_h) rotates counter-clockwise (positive ω_z) in the northern hemisphere and vice versa in the southern hemisphere. These results are in agreement with earlier known rotation properties of supergranular flows (Duvall & Gizon 2000; Gizon & Duvall 2003). Further the magnitudes of ω_z^q derived as above increase more or less linearly against magnitudes of d_h.

Although the above result indicates that the predominant variation of $\omega_z^q(d_h)$ in quiet-Sun flows at the scales that we are measuring is due to the Coriolis effect, it is expected that not all size vortex flows have the signs following the Coriolis effect. In particular, any smaller scale vortex flows at granular inflows or junctions within the supergranular cells can potentially be of larger magnitude and not influenced by the Coriolis force. This

indeed turns out to be true as the averages of absolute values, $\omega_z^{ab}(d_h, B)$ ($H_k^{ab}(d_h, B)$), shown in Figures 6 and 7 portray. The top panels in these figures show the 2D binned maps, while the bottom panels show the non-magnetic $\omega_z^{ab,q}(d_h)$ (blue lines) and averages over a few selected magnetic field ranges (as in Figures 4 and 5) against abs(d_h) for a comparison of outflows and inflows. In the analysis and plots here, the error bars represent standard deviations within the ranges of the magnetic bins used. First, as noted earlier, the magnitudes of vorticities (determined through the averages of absolute values) are about ten times those of the excesses determined to be resulting from the hemispherical preference of one sign over the other due to the Coriolis force (compare the values in Figures 4 and 5 with those in Figures 6 and 7). The magnitudes of vorticities estimated in our work here compare very well with earlier local helioseismic results from Gizon & Duvall (2003) and Duvall & Gizon (2000), and with the local helioseismic as well as LCT analyses of Langfellner et al. (2015). Second, in agreement with the earlier findings (Wang et al. 1995), the inflow regions have slight excess vorticity (and helicity) compared to the outflow regions for non-magnetic flows (the blue curves in Figures 6 and 7). We discuss the magnetic modifications in the following section.

3.2. Magnetic Effects: Transfer and Redistribution of Vorticity

To study how the above described non-magnetic relationship $\omega_z^q(d_h)$ is influenced by the magnetic field, we average $\omega_z(d_h, B)$ and $\omega_z^{ab}(d_h, B)$ (as well as $H_k(d_h, B)$ and $H_k^{ab}(d_h, B)$) over three different ranges of magnetic field: 20–80 G (denoted as 50 G), 150–250 G (denoted as 200 G), and 250–350 G (denoted as 300 G) centered around 50, 200, and 300 G. The results are
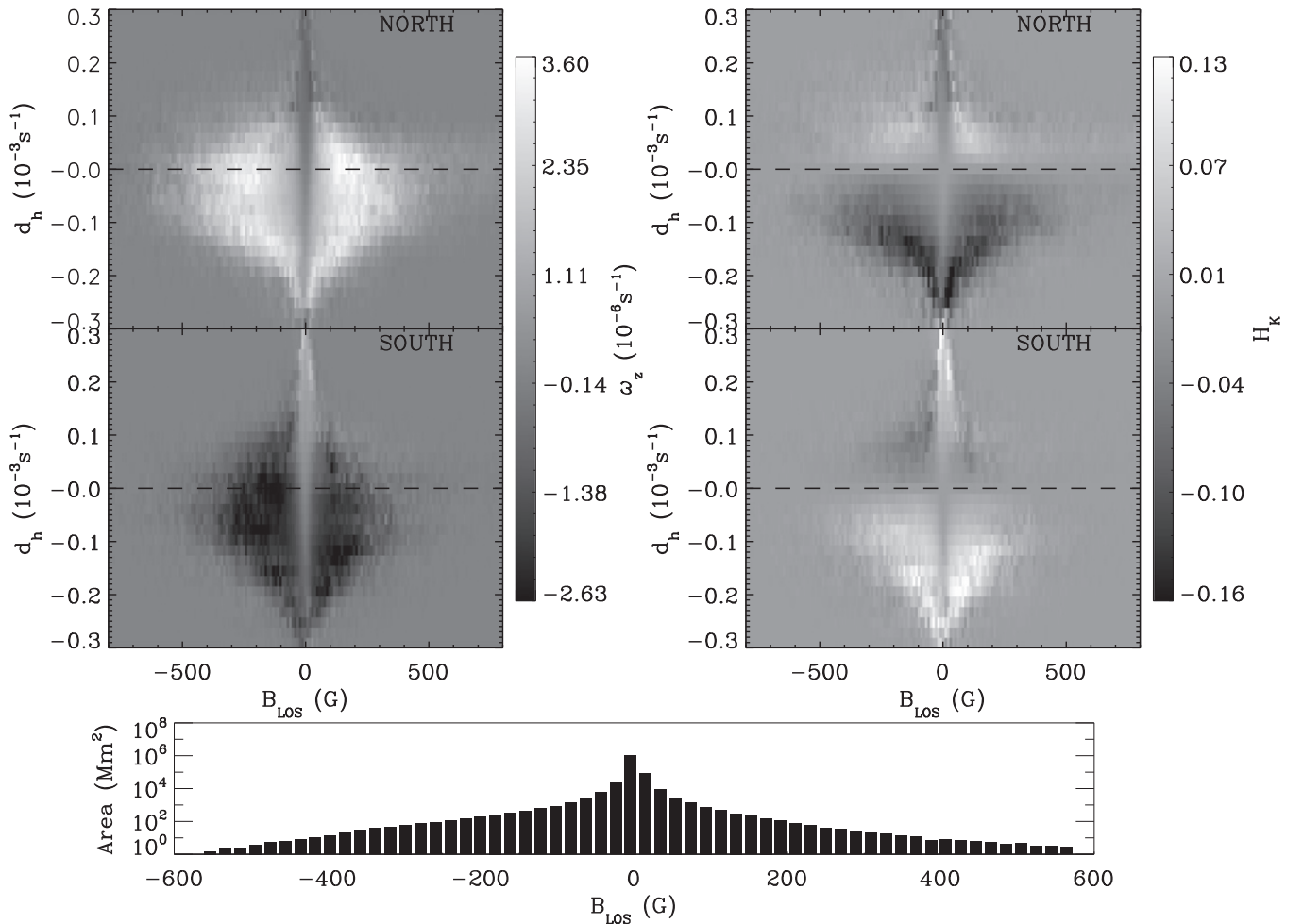
Figure 3. $\omega_z(d_h, B)$ and $H_k(d_h, B)$ are the same as plotted in Figure 2 but are derived from correlation tracking of granular motions imaged in HMI Doppler velocities. The bottom panel shows a histogram of area (in logarithmic scale) occupied by magnetic pixels in units of Mm^2 against $B = B_{LOS}$.

shown in Figures 4–7. First, we see from Figures 2 and 3 that the sign of $\omega_z(d_h, B)$ over the magnetized regions does not follow the dependence on d_h expected from the action of the Coriolis force: while the non-magnetic ($<\pm 10\,G$) central vertical regions of Figures 2 and 3 show the sign change (the blue curves in the left panel of Figure 4) through $d_h = 0$., the magnetized regions show predominantly one sign, i.e., positive in the north and negative in the south, which should hold only for inflows or converging flows (negative d_h) if the Coriolis effect is the cause. However, magnetic fields over outflows or diverging flows (positive d_h) also show the same sign as that seen over converging (negative d_h) regions, although it is noted that the majority of the magnetic fluxes lie over the converging or inflow (negative d_h) regions. It is clear that the dominant inflow located magnetic fields are connected to those located in the interiors of supergranules (with positive d_h), and that such connectivity transfers vorticity from the inflow (negative d_h) regions to fluid surrounding such connected fields within the supergranules (positive d_h). This magnetic connectivity is expected in the predominantly mixed-polarity flux, which can have a large horizontal component or loops arching above the photosphere. This transfer can happen in either direction, but it is seen in Figures 2 and 3 that the transfer of vorticity (and kinetic helicity) is predominantly from inflow regions (negative d_h) to outflows or diverging flows (positive d_h); this is

consistent with the fact that stronger magnetic fields with larger fluxes are found mainly over the inflow regions. The cross-sections over the three different magnetic field ranges plotted in Figures 4–7 show the above described signatures of transfer of vorticity from the inflow to outflow regions more clearly, and also show how the strengths of the magnetic field influence this phenomenon.

We add a caveat here to the above inferences on possible transfer of vorticity from supergranular inflow (negative d_h) to outflow (positive d_h) regions: the rearrangement of magnetic flux during the process of evolution of supergranules, namely "dying" inflow that is replaced by the outflow of a new supergranule, can lead to our analyses finding vorticity in outflow regions that matches the vorticity in inflow regions (as described above). This can arise because the newly formed outflow (in the place of old inflow) has not had time to sweep the flux to the new inflow region and the Coriolis force has also not had time to act and hence reverse the vorticity. However, we note that the averaging over 14 hr, which is more than about half the lifetime of a supergranule and hence is long enough for both the above processes to establish, should tend to smooth out such signatures of dying and newly forming supergranular flows. Nevertheless, a residual signature of this process is certainly possible in our analyses.
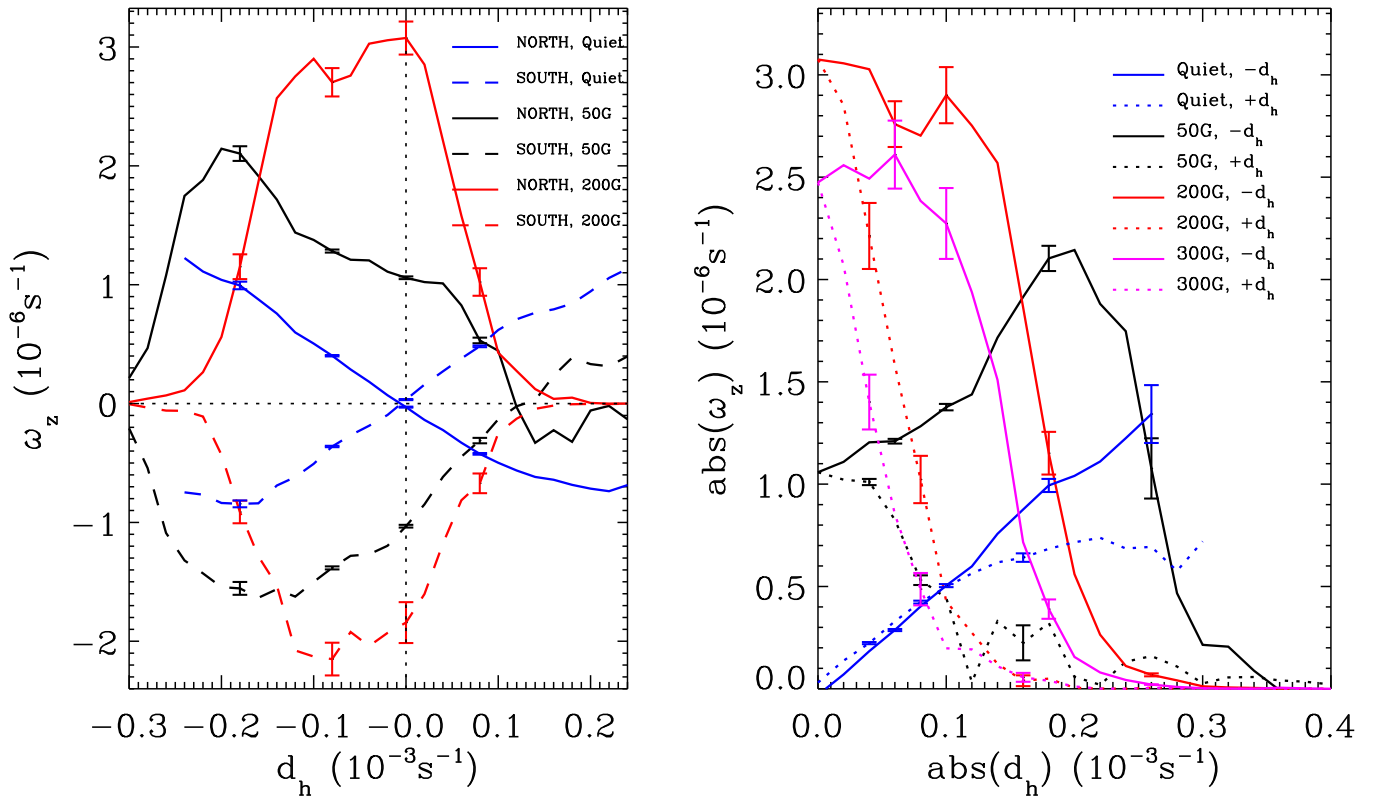
Figure 4. Averages over different field strength ranges, as marked in the panels, of vertical vorticities $\omega_z(d_h, B)$ calculated from results shown in Figure 3. The left panel shows signed ω_z against signed d_h, whereas the right panel shows the magnitudes of these quantities for an easy comparison of inflow (solid curves) and outflow (dotted curves) regions. The 300 G curves added in the right panel are to show that the vorticity values decrease beyond 200 G. They are not shown in the left panel for the sake of clarity as we include both northern and southern hemisphere results in the same plot. For the magnitudes in the right panel, we have used only those for the northern region. See the text for further details.
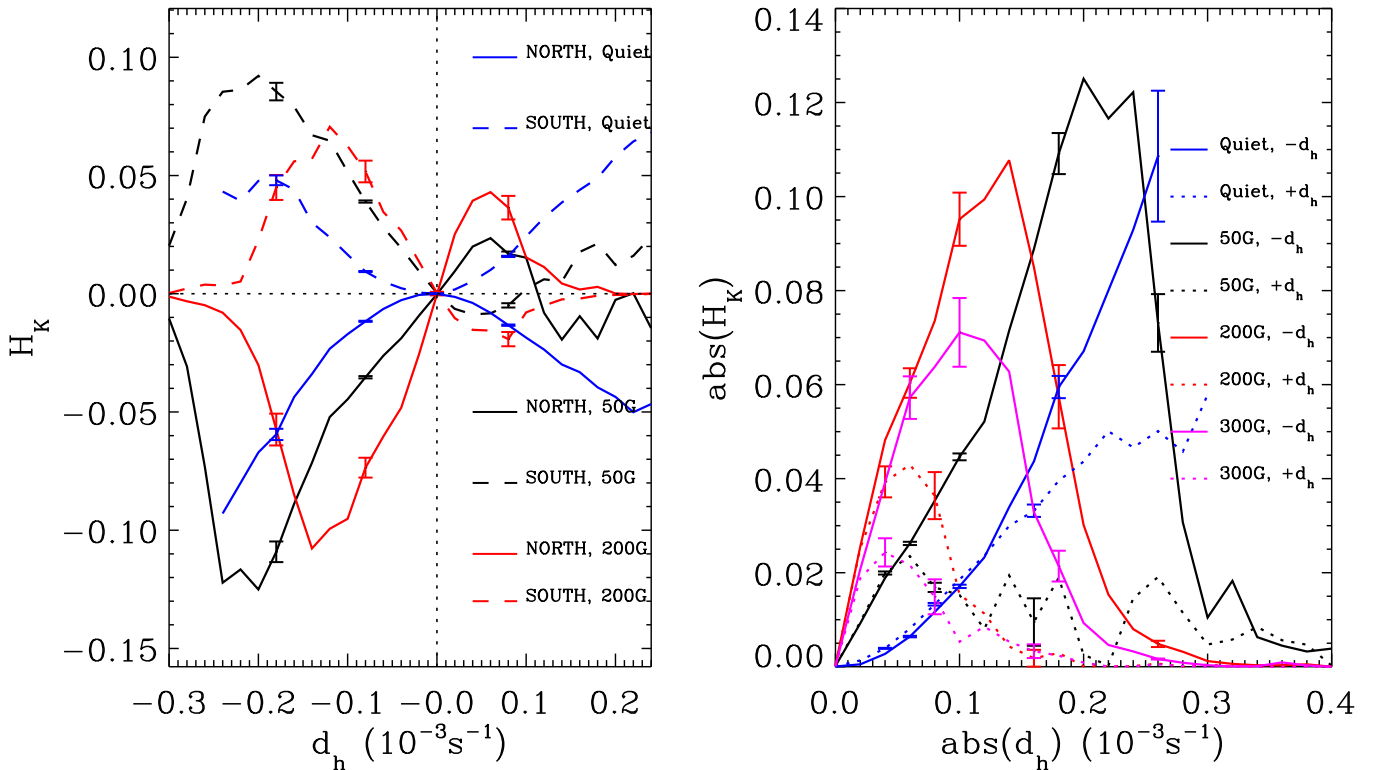
Figure 5. Similar plot to Figure 4 but for signed averages of kinetic helicity, $H_k(d_h, B)$.
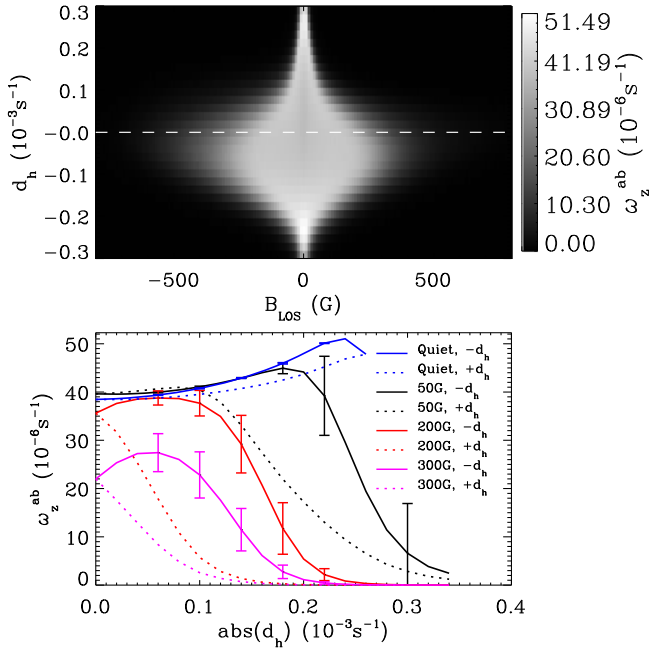
Figure 6. Absolute values of vertical (z-component) vorticity, $\omega_z^{ab}(d_h, B)$ (top panel), binned against LOS magnetic field, B (x-axis), and horizontal divergence, d_h (y-axis). The bottom panel shows the cross-sections averaged over different field strength ranges the same as in the right panel of Figure 4. See the text for further details.
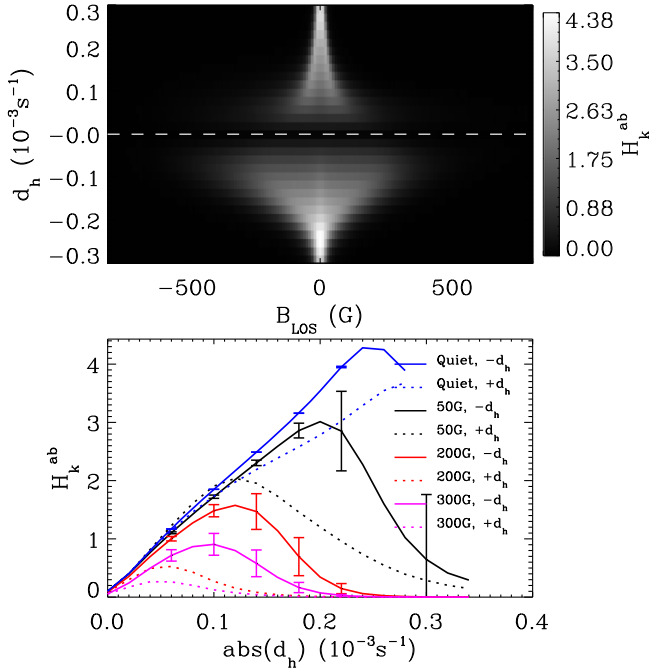

Figure 7. Similar plot to Figure 6 but for averages of absolute values of kinetic helicity, $H_k^{ab}(d_h, B)$.

In addition, we find that these differences between inflow and outflow vorticities (and helicities) are much more pronounced for flows around magnetic fields—see the black (50 G), red (200 G), and pink (300 G) curves in Figures 6 and 7. It is to be noted, however, that these enhanced excesses of inflow vorticities, both in signed averages (Figures 4 and 5) as well as in averages of absolute values (Figures 6 and 7), also depend on the fact that much of the magnetic fields, in

particular stronger concentrations, are located in inflow regions. This is clearly seen in the 2D maps in Figures 2 and 3 and in the top panels of Figures 6 and 7, which show the large asymmetry in the areas occupied by non-zero vorticities in the $B - d_h$ region: relatively weaker fields are found in the supergranular outflows (positive d_h), and the majority of the magnetic flux and stronger field concentrations are in the inflow (negative d_h) regions. A basic feature in all the above magnetic effects is that the linear relationship characterizing $\omega_z^q(d_h)$ has given way to more complicated variations. We present and describe the dependences on the magnetic field strength further in the following section.

3.2.1. Magnetic Suppression of Fluid Vorticity and Helicity

To examine the influence of magnetic field strengths on the sign and amplitudes of ω_z and H_k (Figure 3), and on the absolute magnitudes of ω_z^{ab} and H_k^{ab} (top panels of Figures 6 and 7), we take the averages of these quantities over the divergence bins. These results are shown in Figures 8 and 9. As noted earlier, at $|B| = 0$ G, the opposite contributions to ω_z and H_k from the positive (outflow) and negative (inflow) d_h regions cancel out, yielding near-zero values for these quantities. However, the averages of the absolute values of ω_z^{ab} and H_k^{ab} show that the largest magnitude vorticities are to be found over non-magnetic flows, and they decline sharply as $|B|$ increases. The excesses $\omega_z(B)$ and $H_k(B)$, however, show a rapid increase at low magnetic field strengths, reaching a maximum between about 150 and 200 G. The sign pattern of magnetic field correlated ω_z and H_k preserves that expected from Coriolis force action on inflows (negative d_h regions). Taken together, these results show that a major contribution to the larger magnitudes of vorticities and kinetic helicities in inflow regions, compared to those over diverging flows in the interiors of supergranules, leading to the hemispheric excesses seen in Figure 8 are due to the predominance of magnetic fields at inflow locations. It is also possible that the supergranular inflows have more vigorous swirls around them due to larger thermal perturbations that strong magnetic flux concentrations cause in the solar photospheric layers: cooler magnetic field trapped photospheric gas acts as channels for further heat (radiative) loss, vertically outward accelerating the flows surrounding hotter plasma toward them, thus enabling stronger inflows and vorticities.

As the magnetic field increases further beyond equipartition strength, which is typically about 300–400 G for the solar photosphere, the back-reaction of the magnetic field via the Lorentz force, involving both the pressure and tension forces, acts to inhibit the flows. This effect eventually becomes dominant and acts to compensate the contributions from the Coriolis force assisted combinations of inflows and magnetic fields leading to the decreases seen in Figure 8. As for the averages of absolute magnitudes ω_z^{ab} and H_k^{ab} shown in Figure 9, it is clear that, when we ignore the outflow–inflow asymmetry in the magnetic field locations and the resulting influence of the Coriolis force, the net effect of magnetic forces is to suppress vortical motions. There might also be contributions due to the fact that field strengths B here (from HMI) are flux densities within the resolution element of the instrument, and hence the increase of $|B|$ here may mainly reflect the increase of flux while the actual field strengths are already in strong saturated super-equipartition values. That the photospheric small-scale network field concentrations outlining
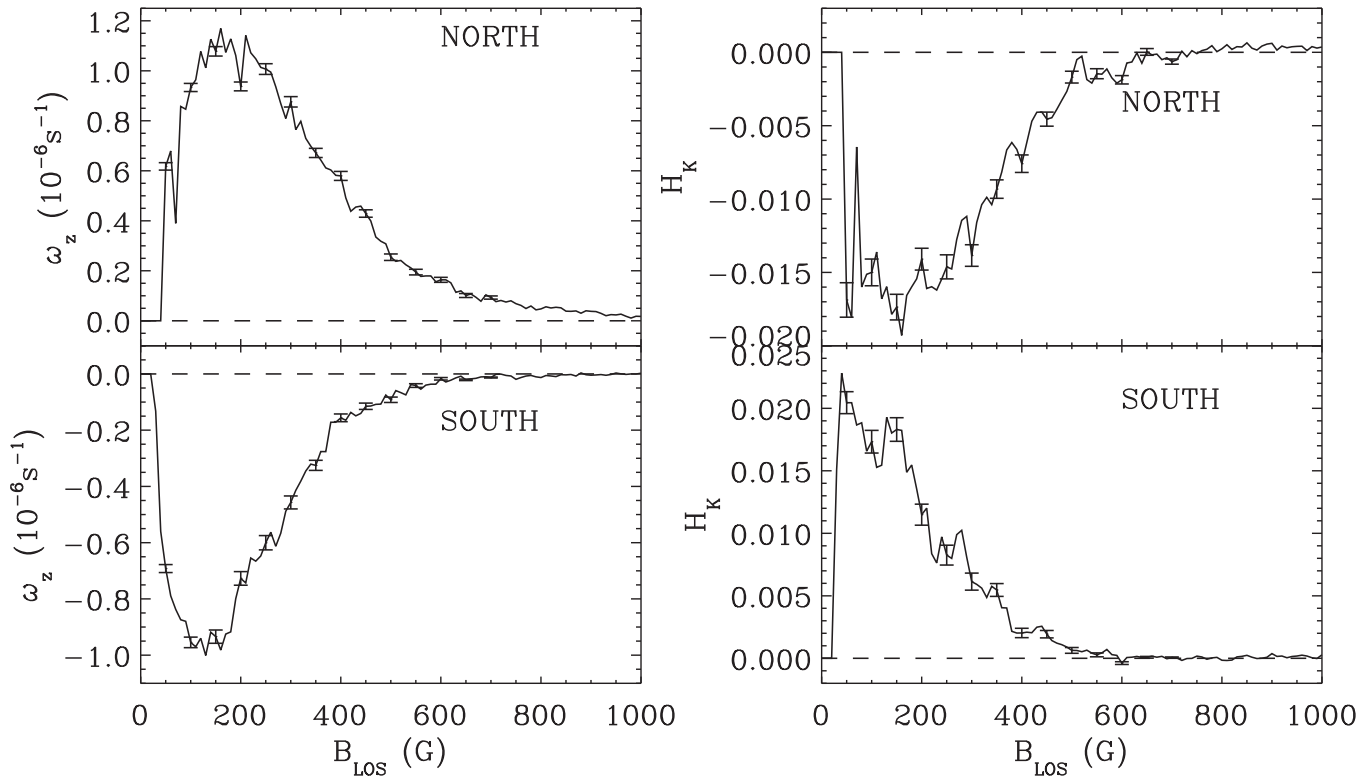
Figure 8. The left panels show vertical vorticities, $\omega_z(B)$, averaged over the divergence bins in Figure 3, plotted against field strength $|B|$ for the northern and southern hemispheres separately. The right panels show the similarly averaged kinetic helicities $H_k(B)$. The error bars represent standard errors estimated from individual measurements. The horizontal dashed lines in the panels mark the zero level of the ordinates.
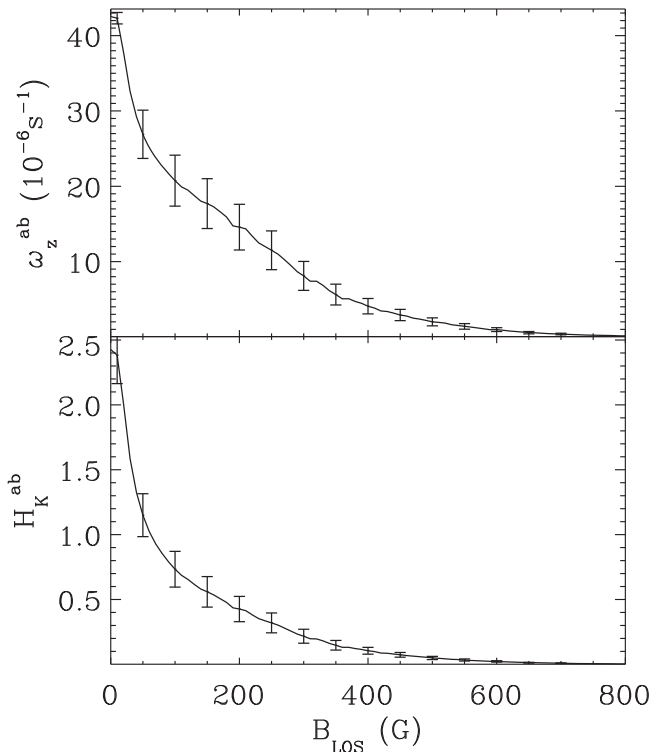

Figure 9. The same as Figure 8, but for averages of absolute vorticities, $\omega_z^{ab}(B)$ (top panel), and kinetic helicities $H_k^{ab}(B)$ (bottom panel). Here, the north and south regions have been averaged together.

supergranular inflows are predominantly of super-equipartition kG field strengths is a well established fact. Hence, the results in Figure 9 for vorticities and kinetic helicities may correspond to the so-called highly α-quenched state, if photospheric flows are considered for a (helical-)turbulent local dynamo (see, e.g., Brandenburg & Subramanian 2005, and references therein). In nonlinear mean-field dynamo theory, both the hydrodynamic (α_k) and magnetic (α_m) parts of the the α-effect are coupled via the magnetic field, and explicit algebraic expressions for the dependences $\alpha_k(B)$ and $\alpha_m(B)$ are available (Rogachevskii & Kleeorin 2000; Zhang et al. 2006). The α_k is proportional to H_k^{ab} shown in Figure 9. However, we note that the theoretical quenching functions that determine $\alpha_k(B)$ are in terms of the mean magnetic field B, which develops out of dynamo action at the small-scale, whereas in our observations and analysis here B refers to the field at the small-scale. A more detailed look at $H_k^{ab}(B)$ or $\alpha_k(B)$, their spectra, both spatial and temporal, and their relations to various other local and global properties of solar magnetic fields in the context of dynamo mechanisms is beyond the scope of the work reported here. Moreover, higher spatial resolution than provided by HMI to resolve sub-granular scale flows and magnetic fields is important to address such details.

4. SUMMARY AND DISCUSSION

We have derived and analyzed horizontal fluid motions on the solar surface over large areas covering the quiet-Sun magnetic network using LCT of convective granules imaged in continuum intensity and Doppler velocity by the HMI on board *SDO*. We have studied the relationships between fluid

divergence and vorticity, and that between vorticity (kinetic helicity) and the magnetic field. These relationships are derived through both signed and absolute averages of ω_z and H_k over time and space. These latter dependences are studied through fluid divergence $d_h(x, y, t)$ and the magnetic field $B(x, y, t)$, yielding $\omega_z(d_h, B)$, $H_k(d_h, B)$, $\omega_z^{ab}(d_h, B)$, and $H_k^{ab}(d_h, B)$ (Figures 2–5). The main results obtained can be summarized as follows.

(1) The correlations between the vorticity and divergence of non-magnetic flows at the supergranular-scale have the dominant hemispheric sign pattern brought about by the action of the Coriolis force. The rotations of outflows and inflows are roughly of equal magnitude and of opposite sign, although there is a slight excess of inflow vorticities which increase as the magnitude of divergence increases. Further, the non-magnetic vorticities scale linearly with the divergences.

(2) For magnetized flows, the sign pattern corresponding to the inflows dominates over the whole divergence field, i.e., even the outflow regions (positive divergence, interiors of supergranules) exhibit the rotations expected from the action of the Coriolis force acting on inflows. In other words, for magnetized flows the dominant sign pattern is negative helicity H_k (positive ω_z) in the north and positive helicity H_k (negative ω_z) in the south. We have identified and attributed this to the mechanism of transfer of vorticity from network inflow regions to interiors of supergranules by the magnetic connectivity or by the horizontal component of magnetic field, with a caveat that supergranular evolution ("dying" inflow that is replaced by the outflow of a new supergranule) can also contribute to the observed signatures.

(3) The excess of inflow vorticities over those of outflows increases dramatically for magnetized flows. This has been identified as being due to the preferential inflow locations of magnetic fields resulting from the convective flux expulsion mechanism. The contributions of intrinsically larger rotations of inflows around stronger fields due to thermal causes, however, can also play a role in the above asymmetries between outflow and inflow rotations.

(4) In terms of the absolute magnitudes of vorticities, it has been found that non-magnetic flows have the largest values. As a function of magnetic field strengths, as observed by HMI, the magnitudes of absolute vorticities decrease almost exponentially, causing the magnetic suppression of flows due to Lorentz forces. In particular, we find that the magnetic fields largely suppress the amplitudes of vortical motions when magnetic flux densities exceed about 300 G (from HMI). This magnetic suppression of vorticities or helicities is identified as that arising from the α-quenching action of the magnetic field. This identification is found to be reasonable as much of the magnetic flux in the solar photosphere is known to be of kG strengths, which are well above the equipartition values.

The above results have wider implications and relations to several other related phenomena pertaining to magneto-convective processes in the solar photosphere. The results (1) and (2) above related to the hemispheric pattern of fluid kinetic helicity and its relationship to the magnetic field are of importance in understanding the transfer of helicities between the fluid and magnetic fields, in particular in situations where reliable measurements of magnetic helicities in the small-scale are difficult to obtain. Since we have not measured magnetic helicities, we cannot establish the connections or transfer of helicities between fluid motions and the magnetic field.

However, if the transfer of helicities happens between fluid motions and the magnetic field, irrespective of which direction it happens, we expect both to have the same sign. In our analysis, we find that kinetic helicity is negative (positive) in the northern (southern) hemisphere and this is consistent with magnetic helicity followed by active regions. On the other hand, if the small-scale fields have the opposite sign of current helicity compared to active regions as reported by Gosain et al. (2013), then the transfer of helicity from fluid motions could not have happened, as this is not consistent with our observations. Thus, if the magnetic helicity of the small-scale magnetic fields all over the Sun has contributions from kinetic helicity, then we expect it to have the same sign as the active regions. Hence, our results indicate that small-scale magnetic helicity would indeed be of the same sign as that of active regions that follow the usual hemispheric trend.

The transfer and redistribution of vorticities by magnetic fields implied by results (2) and (3) exemplify the basic magnetohydrodynamic effect known from early laboratory experiments involving conducting liquid metals performed and expounded by Shercliff (1971). These same laboratory experiments also demonstrate the suppression of swirly motions by the magnetic field, when the field and fluid velocity directions are not aligned. Our result (4) here is an example of this phenomenon on the Sun.

As regards the relevance of our results for understanding the nature of fluid turbulence and the associated dynamo-sustaining state of near-surface convection (Brandenburg & Schmitt 1998; Rudiger 2001), we note that the dominance of negative kinetic helicity in the north, and hence the expected same sign for magnetic helicity, indicate a positive α-effect in the north in contrast to that required for explaining the observed butterfly diagram of large-scale active regions. As referred to earlier, more detailed analyses of the distribution of kinetic helicity, its interactions with the magnetic field, its spatio-temporal spectra, and their relations to various other local and global properties of solar magnetic fields are necessary to make progress toward devising observational diagnostics of possible dynamo actions happening in the near-surface layers. We note that continuous wide field of view observations of higher spatial resolution to resolve sub-granular scale flows and magnetic fields than provided by HMI/*SDO* is important to address such details. We believe that the kind of analyses undertaken here, e.g., such as those derived from the results in Figure 3, as applied to magnetic regions in different dynamical states such as emerging flux regions, decaying active regions, and those before, during, and after major atmospheric activity such as eruptions or flares, would aid in understanding the interactions between fluid and magnetic helicities, their evolution, exchange, and transport upwards in the atmosphere.

REFERENCES

Balmaceda, L., Dominguez, V. S., Palacios, J., et al. 2010, A&A, 513, L6
Berger, M. A., & Field, G. B. 1984, JFM, 147, 133
Bonet, J. A., Marquez, I., Sanchez Almeida, J., et al. 2008, ApJL, 687, 131
Brandenburg, A., Nordlund, A., Stein, R. F., & Torkelsson, U. 1995, ApJ, 446, 741
Brandenburg, A., & Schmitt, D. 1998, A&A, 338, L55
Brandenburg, A., & Subramanian, K. 2005, PhR, 417, 1
Brandt, P. N., Scharmer, G. B., Ferguson, S., et al. 1988, Natur, 335, 238
Duvall, T. L., Jr., & Gizon, L. 2000, SoPh, 192, 177
Gizon, L., & Birch, A. C. 2005, LRSP, 2, 6
Gizon, L., & Duvall, T. L., Jr. 2003, ASP, 517, 43
Goode, P. R., Yurchyshyn, V., Cao, W., et al. 2010, ApJL, 714, L31
Gosain, S., Pevtsov, A. A., Rudenko, G. V., & Anfinogentov, S. A. 2013, ApJ, 772, 52
Hale, G. E. 1927, Natur, 119, 708
Hindman, B. W., Haber, D. A., & Toomre, J. 2009, ApJ, 698, 1749
Hoeksema, J. D., Liu, Y., Hayashi, K., et al. 2014, SoPh, 289, 3483
Innes, D. E., Genetelli, A., Attie, R., & Potts, H. E. 2009, A&A, 495, 319
Komm, R., Gosain, S., & Petsov, A. 2014, SoPh, 289, 475
Komm, R., Howe, R., Hill, F., et al. 2007, ApJ, 667, 571
Krause, F., & Rädler, K.-H. 1980, Mean-field Magnetohydrodynamics and Dynamo Theory (Berlin, Oxford: Akademie-Verlag, Pergamon)
Langfellner, J., Gizon, L., & Birch, A. C. 2015, A&A, 581, 67
Lisle, J., & Toomre, J. 2004, in Proc. SOHO 14/GONG 2004 Workshop, Helio- and Asteroseismology: Toward a Golden Future, ed. D. Dansey (Noordwijk: ESA), 556
Lites, B. W., Kubo, M., Socas-Navarro, H., et al. 2008, ApJ, 672, 1237
Liu, Y., Hoeksema, J. T., Bobra, M., et al. 2014a, ApJ, 785, 13
Liu, Y., Hoeksema, J. T., & Sun, X. 2014b, ApJL, 783, L1
Longcope, G. H., Fisher, G. H., & Pevtsov, A. A. 1998, Geophysical Monographs Series, 111, 93
Moffat, H. K. 1978, Magnetic Field Generation in Electrically Conducting Fluids (Cambridge: Cambridge Univ. Press)
Nordlund, A., Stein, R. F., & Asplund, M. 2009, LRSP, 6, 2
November, L. J., & Simon, G. W. 1988, ApJ, 333, 427
Parker, E. N. 1955, ApJ, 121, 491
Pevtsov, A. A., Canfield, R. C., & Metcalf, T. R. 1995, ApJL, 440, 109
Proctor, M. R. E., & Weiss, N. O. 1982, RPPh, 45, 11
Rajaguru, S. P., Couvidat, S., Sun, X., Hayashi, K., & Schunker, H. 2013, SoPh, 287, 107
Rogachevskii, I., & Kleeorin, N. 2000, PhRvE, 61, 5202
Rudiger, G. 2001, in IAU Symp. 203, Recent Insights into the Physics of the Sun and Heliosphere, ed. P. Brekke, B. Fleck, & J. B. Gurman (San Francisco, CA: ASP), 152
Rudiger, G., Brandenburg, A., & Pipin, V. V. 1999, AN, 320, 135
Rudiger, G., Pipin, V. V., & Belvedere, G. 2001, SoPh, 198, 241
Scherrer, P. H., Schou, J., Bush, R. J., et al. 2012, SoPh, 275, 207
Schou, J., Scherrer, P. H., Bush, R. I., et al. 2012, SoPh, 275, 229
Schussler, M., & Vogler, A. 2008, A&A, 481, L5
Seehafer, N. 1990, SoPh, 125, 219
Shelyag, S., Cally, P. S., Reid, A., & Mathioudakis, M. 2013, ApJL, 776, 4
Shercliff, J. A. 1971, Film Notes for Magnetohydrodynamics, National Committee for Fluid Mechanics Films
Simon, G. W., November, L. J., Ferguson, S. H., et al. 1989, in NATO Advanced Science Institutes (ASI) Ser. C, ed. R. J. Rutten, & G. Severino (Dordrecht: Kluwer), 371
Wang, Y., Noyes, R. W., Tarbell, T. D., & Title, A. M. 1995, ApJ, 447, 419
Wedemeyer-Bohm, S., Scullion, E., Steiner, O., et al. 2012, Natur, 486, 505
Welsch, B. T., Abbett, W. P., De Rosa, M. L., et al. 2007, ApJ, 670, 1434
Welsch, B. T., Fisher, G. H., & Abbett, W. P. 2004, ApJ, 610, 1148
Zhang, H., Sokoloff, D., Rogachevskii, I., et al. 2006, MNRAS, 365, 276
Zhang, M. 2006, ApJL, 646, 85